Chemical Science

ROYAL SOCIETY OF CHEMISTRY

EDGE ARTICLE

Cite this: *Chem. Sci.*, 2020, **11**, 11037

All publication charges for this article have been paid for by the Royal Society of Chemistry

A FRET-based fluorescent Zn^{2+} sensor: 3D ratiometric imaging, flow cytometric tracking and cisplatin-induced Zn^{2+} fluctuation monitoring†

Hongxia Xu,‡[a] Chengcheng Zhu,‡[a] Yuncong Chen, *[ab] Yang Bai,[a] Zhong Han,[a] Shankun Yao,[a] Yang Jiao,[a] Hao Yuan,[a] Weijiang He *[a] and Zijian Guo *[ab]

Received 30th May 2020
Accepted 9th September 2020

DOI: 10.1039/d0sc03037f

rsc.li/chemical-science

Monitoring labile Zn^{2+} homeostasis is of great importance for the study of physiological functions of Zn^{2+} in biological systems. Here we report a novel ratiometric fluorescent Zn^{2+} sensor, CPBT, which was constructed based on chelation-induced alteration of FRET efficiency. CPBT was readily cell membrane permeable and showed a slight preferential localization in the endoplasmic reticulum. With this sensor, 3D ratiometric Zn^{2+} imaging was first realized in the head of zebra fish larvae *via* Z-stack mode. CPBT could track labile Zn^{2+} in a large number of cells through ratiometric flow cytometric assay. More interestingly, both ratiometric fluorescence imaging and flow cytometric assay demonstrated that the labile Zn^{2+} level in MCF-7 cells (cisplatin-sensitive) decreased while that in SKOV3 cells (cisplatin-insensitive) increased after cisplatin treatment, indicating that Zn^{2+} may play an important role in cisplatin induced signaling pathways in these cancer cells.

Introduction

Biological Zn^{2+} is an essential component for many proteins and is involved in various physiological processes such as gene transcription, neurotransmission, DNA repair, cell proliferation, apoptosis and redox responses.[1–5] Disorder in Zn^{2+} homeostasis is associated with neurodegenerative diseases, cancer and immune defects.[6–11] As a powerful technology which can provide spatiotemporal information on Zn^{2+}, fluorescence imaging has been applied in living cells, tissues and model animals.[12–16] Imaging and monitoring labile Zn^{2+} fluctuation is intriguing yet challenging since the deviation of endogenous labile Zn^{2+} homeostasis might be very small and dynamic. Moreover, interference from photobleaching, sensor concentration variation, and light scattering may result in misleading information. Therefore, ratiometric Zn^{2+} imaging is more reliable for accurate Zn^{2+} determination due to the self-calibration effect of dual emission.[17–20]

Much effort has been devoted to ratiometric Zn^{2+} sensors,[21–27] especially small molecule based sensors. Most of them were reported to image exogenous Zn^{2+} loaded into cells, and sensors displaying the ability to image endogenous, labile Zn^{2+} are still highly demanded. Developing ratiometric Zn^{2+} sensors with large emission shifts (>60 nm) and a minimum overlap between two emission bands is challenging yet desirable to improve the detection accuracy and sensitivity. In addition, 3D ratiometric imaging could provide more information on spatial distribution of Zn^{2+}, which is appealing and requires sensors with near infrared (NIR) or two-photon excited fluorescence (TPEF) to improve the tissue penetration depth. Although fluorescence imaging is an ideal technique to provide detailed information on Zn^{2+} distribution in a single cell, it can only observe a limited number of cells in the field of view. In this regard, flow cytometry stands out as an attractive fluorescence technique to monitor Zn^{2+} fluctuations in a large number of cells.[28–30]

Cisplatin, which covalently binds with DNA to induce DNA damage, is one of the most widely used platinum-based antitumor drugs in clinics. Its DNA-adduct has been proposed to trigger pathways such as ATR, p53, p73, and MAPK to induce tumor cell apoptosis.[31] Zn^{2+} has been proposed to be involved in many of these pathways, including the p53 pathway.[10,32,33] Zinc deficiency may not only induce an increase in oxidative stress that causes DNA damage but also affect the expression of DNA-repair protein apurinic endonuclease (APE) and the downstream signaling events.[9,34] We envisioned that intracellular Zn^{2+} homeostasis would be disturbed by cisplatin treatment, and different Zn^{2+} responses may be related to the sensitivity of cancer cells to cisplatin. Therefore, temporal monitoring of cisplatin-triggered labile Zn^{2+} fluctuations in different cancer cells is of great significance for the study of

[a]*State Key Laboratory of Coordination Chemistry, Coordination Chemistry Institute, School of Chemistry and Chemical Engineering, Nanjing University, Nanjing 210023, P. R. China. E-mail: chenyc@nju.edu.cn; heweij69@nju.edu.cn; zguo@nju.edu.cn*

[b]*Chemistry and Biomedicine Innovation Center, Nanjing University, Nanjing 210023, P. R. China*

† Electronic supplementary information (ESI) available. See DOI: 10.1039/d0sc03037f

‡ These authors contributed equally to this work.

Zn^{2+} physiology during cisplatin-induced DNA damage, which may shed some light on the future development of new anti-cancer drugs.

Herein, we report a novel FRET-based ratiometric Zn^{2+} sensor, CPBT, which is constructed by integrating a two-photon excitable coumarin derivative with an intramolecular charge transfer (ICT) fluorophore 4-amine-7-sulfamoylbenzo[*c*][1,2,5]-oxadiazole (ASBD). The electron donating group (4-amino group) of the ASBD fluorophore was modified with the Zn^{2+} ionophore *N*,*N*,*N*′-tri(pyridin-2-ylmethyl)ethane-1,2-diamine (TPEA), and Zn^{2+} binding would decrease the electron-donating ability of the 4-amino group and weaken the ICT effect in the ASBD fluorophore. A distinct blue shift of ASBD absorption would be observed due to Zn^{2+}-chelation-induced alteration of the ICT effect.[24,35] We envisioned that the large blue shift would diminish the spectral-overlap between donor emission and acceptor absorption, leading to a significant decrease in the FRET efficiency of CPBT (Fig. 1a). CPBT showed a specific Zn^{2+}-induced large emission blue shift of ~80 nm. Besides 2D ratiometric imaging, 3D ratiometric mapping of endogenous labile Zn^{2+} distribution in the head of zebrafish larvae was realized using CPBT. In addition, detection of endogenous labile Zn^{2+} in a large number of cells was achieved by ratiometric flow cytometry. More interestingly, both ratiometric fluorescence imaging and flow cytometric assay demonstrated an opposite change of labile Zn^{2+} in cisplatin-sensitive MCF-7 (human breast cancer cell line, Zn^{2+} decrease) and cisplatin-insensitive SKOV3 (human ovarian cancer cell line, Zn^{2+} increase) after cisplatin treatment. Considering the involvement of Zn^{2+} in cisplatin-related cell apoptosis pathways such as p53 and DNA damage repair, the current results might offer new clues to clarify the antitumor mechanism of cisplatin and the related drug resistance.

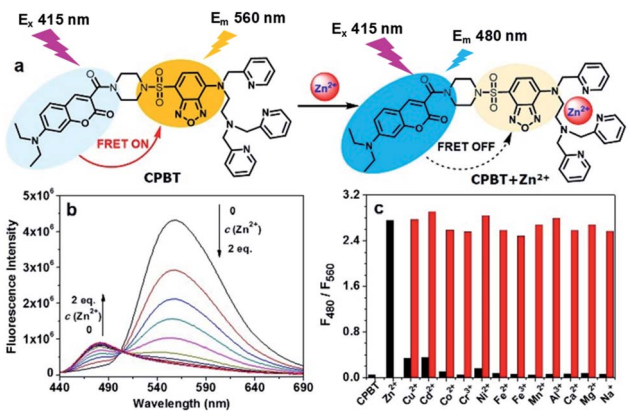

Fig. 1 (a) Chemical structure of CPBT and schematic illustration of its ratiometric Zn^{2+} sensing mechanism. (b) Fluorescence spectra of CPBT (5 μM) in HEPES buffer (containing 1% DMSO) upon Zn^{2+} titration (0–2.0 equiv.). λ_{ex}, 415 nm. (c) Histogram of the ratio of emission at 480 to 560 nm, F_{480}/F_{560}, of CPBT (5 μM) in HEPES buffer induced by different metal ions (Zn^{2+}, Cu^{2+}, Cd^{2+}, Co^{2+}, Cr^{3+}, Ni^{2+}, Fe^{2+}, Fe^{3+}, Mn^{2+} or Al^{3+}, 1 equiv.; Na^{+}, Ca^{2+} or Mg^{2+}, 1000 equiv.). Black bar: the ratios of the sensor in the absence and presence of different cations.

Results and discussion

Synthesis and characterization

CPBT was synthesized from coumarin-2-carboxylic acid in a 4-step procedure (Scheme S1†) and fully characterized by ^{1}H NMR, ^{13}C NMR and HRMS (see ESI†). Compounds **2** and **3** were prepared as the analogues of the donor and acceptor fluorophores in CPBT for comparison.

Spectroscopic study and Zn^{2+}-sensing behaviour of CPBT

The distinct overlap between donor (coumarin) emission and acceptor (ASBD) absorption suggested a high FRET efficiency of CPBT, which was confirmed by the strong emission at 560 nm and weak emission at 480 nm (Fig. 1b, S4a and b†). After Zn^{2+} binding, the absorption spectra of the ASBD moiety showed a large blue shift due to the decreased ICT effect (Fig. S4b and c†), leading to a dramatic decrease in the spectral-overlap and FRET efficiency. As a result, with the increasing concentration of Zn^{2+}, the emission intensity at 560 nm significantly decreased and that at 480 nm increased distinctly. The intensity ratio of F_{480}/F_{560} increased with the decrease of FRET efficiency. Two emission bands are well separated, which is beneficial for larger enhancement of the emission ratio and more accurate Zn^{2+} sensing. The absorption titration assay suggested a 1 : 1 stoichiometry between CPBT and Zn^{2+} (Fig. S4d†). As shown in Fig. 1c, Zn^{2+} treatment induced a large fluorescence intensity ratio enhancement from 0.053 to 2.76, while other metal ions showed negligible effect on the emission ratio. Only small enhancements are induced by biologically scarce metals Cd^{2+} and Cu^{2+}, which will not cause significant interference with Zn^{2+} sensing in biological samples. Moreover, the ratiometric Zn^{2+} sensing ability was intact in the presence of other metal ions. The results indicated that CPBT showed highly specific ratiometric Zn^{2+} sensing ability. In addition, the emission ratios of F_{480}/F_{560} for both the free sensor and Zn^{2+}-bound CPBT were stable in the pH range from 4.5 to 8.0, suggesting that the Zn^{2+} sensing behavior of CPBT could function well in the physiological pH range (Fig. S5†). The K_d value of the Zn^{2+}/CPBT complex was determined to be 14 pM in a competitive binding experiment (Fig. S6†), indicating the high sensitivity of CPBT to Zn^{2+}. The two-photon absorption cross-section is over 40 GM at 780–830 nm (Fig. S7†), indicating that CPBT might be suitable for two-photon excited fluorescence imaging.

2D fluorescence imaging of Zn^{2+} in cells and zebrafish larvae

The desirable ratiometric Zn^{2+} sensing performance in a buffered solution encouraged us to evaluate its Zn^{2+} imaging ability in biological samples. 2D ratiometric Zn^{2+} imaging in living cells was conducted using fluorescence laser scanning confocal microscopy (LSCM). CPBT was readily cell membrane permeable and a co-localization assay showed that CPBT preferentially localized in the endoplasmic reticulum (Fig. S8†). As shown in Fig. 2a–c and S9†, CPBT stained MCF-7 cells displayed a dark-blue ratiometric image, which turned to a green-yellow color after exogenous Zn^{2+} treatment and back to a dark-blue color after incubation with Zn^{2+} scavenger *N*,*N*,*N*′,*N*′-tetrakis(2-pyridylmethyl)ethylenediamine (TPEN). The results indicated

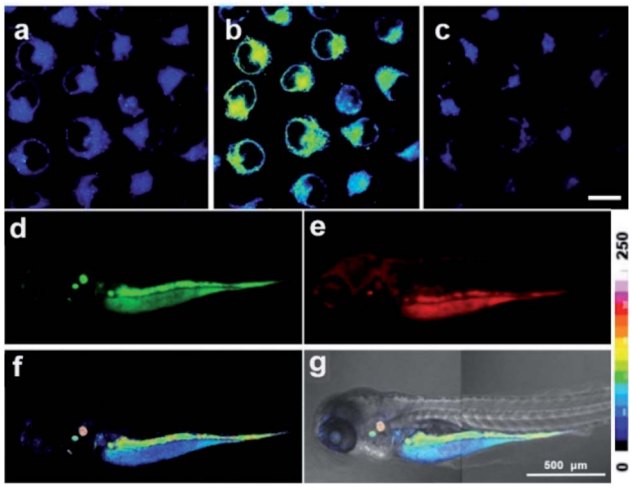

Fig. 2 (a–c) Ratiometric images of MCF-7 cells stained with CPBT (10 μM, 30 min) in the (a) absence and (b) presence of Zn^{2+} (20 μM $ZnCl_2$/pyrithione, 1 : 1, 30 min), and then (c) incubated with 20 μM TPEN for 30 min. Scale bar in (c), 20 μm. (d–g) *In vivo* ratiometric imaging of Zn^{2+} in a 3 day-old zebrafish larva incubated with 0.1 μM CPBT (12 h, 28 °C). (d–f) Images from (d) green channel, (e) red channel and (f) ratiometric channel. (g) Overlay of the ratiometric image and the bright field image. Due to the limited field of view of the instrument, the whole body image for the larva was obtained by combining two images captured under the same imaging conditions. All the ratiometric images were generated from the ratio of green channel (wavelength 440–500 nm) to red channel (wavelength 540–600 nm), λ_{ex} 405 nm. The colour strip is the ratio bar for (a–c), (f) and (g).

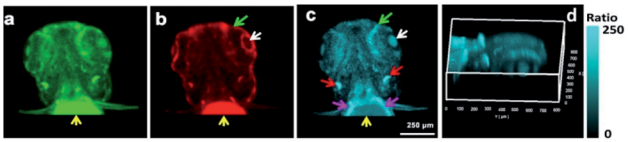

Fig. 3 (a–d) *In vivo* 3D ratiometric imaging of Zn^{2+} fluorescence in the head of a 3 day-old zebrafish larva incubated with 0.1 μM CPBT for 12 h at 28 °C. (a) Top view of the 3D fluorescence image reconstructed from a group of green channel images (440–500 nm); (b) top view of the 3D fluorescence image reconstructed from a group of red channel images (540–600 nm); (c) top view of the 3D ratiometric image reconstructed from a group of ratiometric images; and (d) side view of the reconstructed ratiometric image. All the ratiometric images were generated from the ratio of green channel to red channel. The color strip is the ratio bar for (c) and (d). λ_{ex}, 405 nm.

that the level of labile Zn^{2+} in the cytosol could be elevated by Zn^{2+} incubation and decreased by TPEN treatment. In addition, the chelatable [Zn^{2+}] content in the cytoplasm of MCF-7 cells was estimated to be around 4.2 pM (Fig. 2a and S9j†). CPBT exhibits similar intracellular distribution patterns and ratiometric Zn^{2+} imaging performance in other cell lines, such as A549, SGC-7901, and SKOV3 cells, indicating that this sensor is a suitable candidate to monitor fluctuations in labile Zn^{2+} levels in live cells (Fig. S10 and S11†). Next, the *in vivo* ratiometric mapping of endogenous labile Zn^{2+} in zebrafish larvae was performed by LSCM (Fig. 2d–g). 3 day-old larvae were incubated with CPBT (0.1 μM) for 12 h. The fluorescence image of the red channel showed that CPBT dispersed mostly in the abdomen and parts of the head and trunk, while the images of the green channel showed only limited bright regions. The colors from blue to light red in the ratiometric channel correspond to different levels of endogenous labile Zn^{2+}. The highest labile Zn^{2+} level was observed around the ears, similar to literature reports showing that uniquely high concentrations of synaptic Zn^{2+} were found in the dorsal cochlear nucleus of rats.[36–38]

3D fluorescence imaging of Zn^{2+}

The 2D confocal imaging only shows the Zn^{2+} distribution in a specific focal plane, which is insufficient to disclose the overall spatial fluctuations in Zn^{2+} levels in living systems.[39,40] Therefore, *in vivo* 3D ratiometric imaging of Zn^{2+} levels in the head of zebrafish larvae was performed for the first time using Z-stack mode with an effective imaging depth of ~150 μm (Fig. S12†). Different distribution patterns of the 3D fluorescence and ratiometric images are observed (Fig. 3a–d). Both the top and side views of the 3D ratiometric image indicate that the highest level of labile Zn^{2+} is observed in the ears (red arrows in Fig. 3c) and the upper front superficial region of the yolk sac (magenta arrows in Fig. 3c). Moreover, the specific distribution pattern of labile Zn^{2+} in the eyeball demonstrated that the central pupil with a higher Zn^{2+} level (white arrows in Fig. 3c) is encircled by a dark ring representing a low Zn^{2+} level. The exterior represents the periphery and bottom of the eyeball, which are interspersed with a few regions with high Zn^{2+} levels that form an exterior ring (green arrow in Fig. 3c). These observations suggest that Zn^{2+} may play important roles in auditory and visual signal transduction. The results confirmed that compared with 2D ratiometric imaging, 3D ratiometric imaging could provide much more spatial information on the labile Zn^{2+} distribution in biological samples.

Ratiometric flow cytometric assay for labile Zn^{2+} in live cells

Flow cytometry is an invasive fluorescence technique to monitor Zn^{2+} fluctuations in a large number of cells, while fluorescence imaging can only observe a limited number of cells. However, the reports for ratiometric flow cytometric assay of Zn^{2+} levels are rare. Based on the successful ratiometric Zn^{2+} imaging with CPBT, we adopted a ratiometric flow cytometry protocol through CPBT staining to track the intracellular Zn^{2+} fluctuations in a large number of cells (Fig. 4 and S13†). The dual channel flow cytometric mode with a green channel of 450 ± 25 nm and a red channel of 570 ± 15 nm was adopted to determine the Zn^{2+}-bound sensor (F_G) and free sensor (F_R) emission in each cell. The average F_G/F_R ratio of CPBT stained SKOV3 cells increased from 0.72 to 0.75 after Zn^{2+} treatment and then decreased to 0.46 upon TPEN treatment (Fig. 4a).

To monitor the Zn^{2+} fluctuation in a more intuitive manner, we proposed a novel cell population contour plot method. The contour plot for the cell population is readily produced from the double-staining flow cytometry assay by treating the green and red channel as the emissions from the Zn^{2+}-bound form and free sensor, respectively. A straight line crosses all the contour

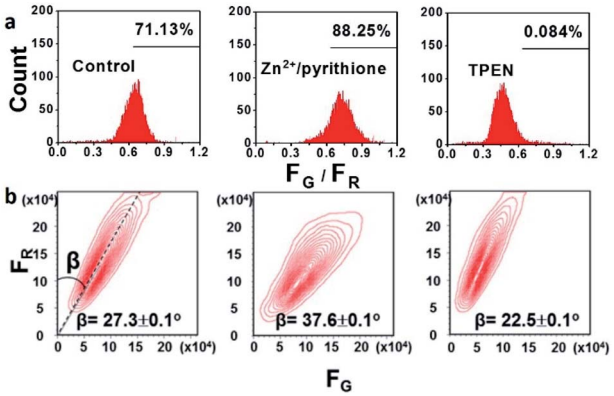

Fig. 4 (a) Cell distribution pattern of SKOV3 cells determined in the dual channel ratiometric flow cytometric assay for intracellular endogenous labile Zn^{2+} according to the average F_G/F_R ratio. Red channel, 570 ± 15 nm, and green channel, 450 ± 25 nm. F_G and F_R are fluorescence intensities detected from green and red channels, respectively. The percentages indicate the proportion of cells with F_G/F_R higher than 0.6. (b) Cell population contour plots (F_G–F_R coordinates) of SKOV3 cells. λ_{ex}, 405 nm; cell number, 10 000.

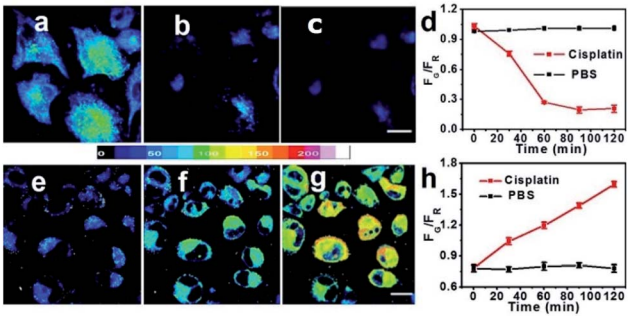

Fig. 5 Ratiometric fluorescence images of CPBT (10 μM, 1 h, 25 °C) stained MCF-7 cells (a–c) and SKOV3 cells (e–g) incubated with cisplatin (20 μM, 25 °C) at 0 h (a and e), 1 h (b and f), and 2 h (c and g) and the temporal profiles ((d) MCF-7 cells; (h) SKOV3 cells incubated with PBS1× or cisplatin) of the average intracellular emission ratio (F_G/F_R) of green channel (F_G, wavelength 440–500 nm) to red channel (F_R, wavelength 540–600 nm) intensity. Ratiometric fluorescence images were generated from the ratio of green channel to red channel. λ_{ex}, 405 nm; scale bar, 10 μm.

lines and forms an angle (β) with the longitudinal coordinate, and the tangent of the angle β is exactly the F_G/F_R ratio. Therefore, the fluctuation of labile Zn^{2+} levels could be estimated by the change of the β angle. The β angle of SKOV3 cells increases from 27.3 ± 0.1° to 37.6 ± 0.1° by Zn^{2+} treatment and decreases to 22.5 ± 0.1° upon TPEN treatment (Fig. 4b). Thus, ratiometric flow cytometry using CPBT staining is an effective technique for determining the intracellular labile Zn^{2+} levels and the β angle analysis of the cell number contour map in F_G–F_R coordinates is a feasible method for estimating the Zn^{2+} levels in different batches of cells.

Tracking of endogenous labile Zn^{2+} fluctuation in cisplatin-treated MCF-7 and SKOV3 cells

Cisplatin is one of the most widely used clinical antitumor drugs to induce DNA damage to cancer cells, while Zn^{2+} has been proposed to be associated with different pathways related to DNA damage repair. Therefore, we try to evaluate whether CPBT is able to monitor the fluctuation of endogenous labile Zn^{2+} induced by cisplatin-stimuli. Ratiometric imaging assay was conducted first, and the CPBT-stained (10 μM, 1 h, 25 °C) cells were treated with cisplatin (20 μM, 25 °C) containing PBS (Fig. 5 and S14–17†). For the MCF-7 cells, the average ratio profile (F_G/F_R) indicated that the labile Zn^{2+} level decreased in the initial 60 min upon cisplatin treatment and remained at a low level thereafter (Fig. 5a–d). However, the labile Zn^{2+} level in SKOV3 cells showed a gradual enhancement at a stable rate in the initial 2 h of cisplatin incubation (Fig. 5e–h). Similar trends were also observed using commercial available Zn^{2+} sensor FluoZin-3 (Fig. S18 and S19†). The ratiometric response could be reversed by addition of Zn^{2+} for MCF-7 cells and pretreatment with TPEN for SKOV3 cells (Fig. S20†). Flow cytometry assay was conducted using a cell culture medium, and labile Zn^{2+} decrease in MCF-7 cells and increase in SKOV3 cells upon cisplatin treatment were observed with an obvious delay in the response time (Fig. S21–S27†). The β angle of MCF-7 cells suggested a steady decrease in the labile Zn^{2+} level in the initial 8 h of cisplatin incubation, while SKOV3 cells exhibited a gradual increase in labile Zn^{2+} levels during the cisplatin incubation of 10 h. The distinct difference of labile Zn^{2+} change in MCF-7 and SKOV3 cells induced by cisplatin incubation might be correlated with their different sensitivities to cisplatin. MCF-7 cells are cisplatin sensitive with an IC_{50} value of 5.7 ± 0.2 μM, while SKOV3 cells are cisplatin insensitive with an IC_{50} value of 42.5 ± 0.7 μM. The cell toxicity of CPBT was also evaluated, the result demonstrated that over 90% of the MCF-7 cells remain viable even for 40 μM CPBT incubation (Fig. S28†). The results suggested that high levels of labile Zn^{2+} might be beneficial for cisplatin resistance, which is in accordance with reports showing that Zn^{2+} is involved in the DNA damage repair pathway.[34,41]

Conclusions

In summary, we have developed a ratiometric sensor for labile Zn^{2+} based on the Zn^{2+}-induced 'on–off' switch of the FRET process. CPBT showed a good separation (80 nm) of the two emission bands, high specificity and affinity to Zn^{2+}. Besides the 2D ratiometric Zn^{2+} imaging in living cells and the zebrafish, 3D ratiometric mapping of endogenous labile Zn^{2+} distribution in the head of zebrafish larvae was realized. In addition, a novel ratiometric flow cytometry assay was successfully applied for tracking endogenous labile Zn^{2+}. More importantly, the cisplatin induced labile Zn^{2+} change was monitored using CPBT. Both ratiometric fluorescence imaging and flow cytometric assay showed that the labile Zn^{2+} level in MCF-7 cells (cisplatin-sensitive) decreased while that in SKOV3 cells (cisplatin-insensitive) increased after cisplatin treatment, confirming that Zn^{2+} plays an important role in the DNA repair in cancer cells. Further in-depth investigation to explore the impact of cisplatin on labile Zn^{2+} fluctuation and the downstream signaling pathways to apoptosis is undergoing in our

lab. This study not only provided a novel and reliable design strategy for the development of Zn^{2+} ratiometric sensors, but also offered new ratiometric protocols for monitoring labile Zn^{2+} homeostasis, which would be beneficial for further exploration of Zn^{2+} biology.

Conflicts of interest

There are no conflicts to declare.

Acknowledgements

This work was financially supported by the National Natural Science Foundation of China (grant no. 21977044, 21907050, 21731004 and 91953201), the Natural Science Foundation of Jiangsu Province (BK20190282), and the Excellent Research Program of Nanjing University (ZYJH004).

Notes and references

1 J. M. Berg and Y. Shi, *Science*, 1996, **271**, 1081–1085.
2 T. V. O'Halloran, *Science*, 1993, **261**, 715–725.
3 S. C. Burdette and S. J. Lippard, *Proc. Natl. Acad. Sci. U. S. A.*, 2003, **100**, 3605–3610.
4 P. I. Oteiza, *Free Radical Biol. Med.*, 2012, **53**, 1748–1759.
5 M. Murakami and T. Hirano, *Cancer Sci.*, 2008, **99**, 1515–1522.
6 C. J. Frederickson, J.-Y. Koh and A. I. Bush, *Nat. Rev. Neurosci.*, 2005, **6**, 449–462.
7 Y. Li, L. Andereggen, K. Yuki, K. Omura, Y. Yin, H. Y. Gilbert, B. Erdogan, M. S. Asdourian, C. Shrock, S. de Lima, U. P. Apfel, Y. Zhuo, M. Hershfinkel, S. J. Lippard, P. A. Rosenberg and L. Benowitz, *Proc. Natl. Acad. Sci. U. S. A.*, 2017, **114**, E209–E218.
8 S. N. Loh, *Metallomics*, 2010, **2**, 442–449.
9 E. Ho, *J. Nutr. Biochem.*, 2004, **15**, 572–578.
10 J. J. Miller, A. Blanchet, C. Orvain, L. Nouchikian, Y. Reviriot, R. M. Clarke, D. Martelino, D. Wilson, C. Gaiddon and T. Storr, *Chem. Sci.*, 2019, **10**, 10802–10814.
11 L. Rink and H. Haase, *Trends Immunol.*, 2007, **28**, 1–4.
12 E. L. Que, R. Bleher, F. E. Duncan, B. Y. Kong, S. C. Gleber, S. Vogt, S. Chen, S. A. Garwin, A. R. Bayer, V. P. Dravid, T. K. Woodruff and T. V. O'Halloran, *Nat. Chem.*, 2015, **7**, 130–139.
13 J. M. Goldberg, F. Wang, C. D. Sessler, N. W. Vogler, D. Y. Zhang, W. H. Loucks, T. Tzounopoulos and S. J. Lippard, *J. Am. Chem. Soc.*, 2018, **140**, 2020–2023.
14 Y. Chen, Y. Bai, Z. Han, W. He and Z. Guo, *Chem. Soc. Rev.*, 2015, **44**, 4517–4546.
15 C. Du, S. Fu, X. Wang, A. C. Sedgwick, W. Zhen, M. Li, X. Li, J. Zhou, Z. Wang, H. Wang and J. L. Sessler, *Chem. Sci.*, 2019, **10**, 5699–5704.
16 L. Fang, G. Trigiante, R. Crespo-Otero, C. S. Hawes, M. P. Philpott, C. R. Jones and M. Watkinson, *Chem. Sci.*, 2019, **10**, 10881–10887.
17 Z. Liu, W. He and Z. Guo, *Chem. Soc. Rev.*, 2013, **42**, 1568–1600.
18 G. Grynkiewicz, M. Poenie and R. Y. Tsien, *J. Biol. Chem.*, 1985, **260**, 3440–3450.
19 Z.-X. Han, X.-B. Zhang, Z. Li, Y.-J. Gong, X.-Y. Wu, Z. Jin, C.-M. He, L.-X. Jian, J. Zhang, G.-L. Shen and R.-Q. Yu, *Anal. Chem.*, 2010, **82**, 3108–3113.
20 K. Sreenath, Z. Yuan, J. R. Allen, M. W. Davidson and L. Zhu, *Chem.–Eur. J.*, 2015, **21**, 867–874.
21 K. Komatsu, Y. Urano, H. Kojima and T. Nagano, *J. Am. Chem. Soc.*, 2007, **129**, 13447–13454.
22 Y. Qin, P. J. Dittmer, J. G. Park, K. B. Jansen and A. E. Palmer, *Proc. Natl. Acad. Sci. U. S. A.*, 2011, **108**, 7351–7356.
23 J. L. Vinkenborg, T. J. Nicolson, E. A. Bellomo, M. S. Koay, G. A. Rutter and M. Merkx, *Nat. Methods*, 2009, **6**, 737–740.
24 Z. Liu, C. Zhang, Y. Chen, W. He and Z. Guo, *Chem. Commun.*, 2012, **48**, 8365–8367.
25 C. J. Chang, J. Jaworski, E. M. Nolan, M. Sheng and S. J. Lippard, *Proc. Natl. Acad. Sci. U. S. A.*, 2004, **101**, 1129–1134.
26 Z. Xu, K.-H. Baek, H. N. Kim, J. Cui, X. Qian, D. R. Spring, I. Shin and J. Yoon, *J. Am. Chem. Soc.*, 2010, **132**, 601–610.
27 M. L. Zastrow, Z. Huang and S. J. Lippard, *ACS Chem. Biol.*, 2020, **15**, 396–406.
28 H. Haase, S. Hebel, G. Engelhardt and L. Rink, *Anal. Biochem.*, 2006, **352**, 222–230.
29 D. Berendji, V. Kolb-Bachofen, K. L. Meyer, O. Grapenthin, H. Weber, V. Wahn and K.-D. Kröncke, *FEBS Lett.*, 1997, **405**, 37–41.
30 B. L. Fiedler, S. Van Buskirk, K. P. Carter, Y. Qin, M. C. Carpenter, A. E. Palmer and R. Jimenez, *Anal. Chem.*, 2017, **89**, 711–719.
31 D. Wang and S. J. Lippard, *Nat. Rev. Drug. Discovery*, 2005, **4**, 307–320.
32 N. Habel, Z. Hamidouche, I. Girault, A. Patiño-García, F. Lecanda, P. J. Marie and O. Fromigué, *Cell Death Dis.*, 2013, **4**, e874.
33 E. Ho, C. Courtemanche and B. N. Ames, *J. Nutr.*, 2003, **133**, 2543–2548.
34 E. Ho and B. N. Ames, *Proc. Natl. Acad. Sci. U. S. A.*, 2002, **99**, 16770–16775.
35 Z. Liu, C. Zhang, Y. Chen, F. Qian, Y. Bai, W. He and Z. Guo, *Chem. Commun.*, 2014, **50**, 1253–1255.
36 S. A. Kodirov, S. Takizawa, J. Joseph, E. R. Kandel, G. P. Shumyatsky and V. Y. Bolshakov, *Proc. Natl. Acad. Sci. U. S. A.*, 2006, **103**, 15218–15223.
37 A. Riccio, Y. Li, J. Moon, K. S. Kim, K. S. Smith, U. Rudolph, S. Gapon, G. L. Yao, E. Tsvetkov, S. J. Rodig, A. Van't Veer, E. G. Meloni, W. A. Carlezon, V. Y. Bolshakov and D. E. Clapham, *Cell*, 2009, **137**, 761–772.
38 S. R. Wegst-Uhrich, E. J. Mullin, D. L. Ding, S. Manohar, R. Salvi, D. S. Aga and J. A. Roth, *BioMetals*, 2015, **28**, 187–196.
39 F. Qian, C. Zhang, Y. Zhang, W. He, X. Gao, P. Hu and Z. Guo, *J. Am. Chem. Soc.*, 2009, **131**, 1460–1468.
40 Z. Guo, G.-H. Kim, J. Yoon and I. Shin, *Nat. Protoc.*, 2014, **9**, 1245–1254.
41 Y. Song, S. W. Leonard, M. G. Traber and E. Ho, *J. Nutr.*, 2009, **139**, 1626–1631.